Hillslopes Record the Growth and Decay of Landscapes

Martin D. Hurst *et al.*

Science **341**, 868 (2013);
DOI: 10.1126/science.1241791

Science (print ISSN 0036-8075; online ISSN 1095-9203) is published weekly, except the last week in December, by the American Association for the Advancement of Science, 1200 New York Avenue NW, Washington, DC 20005.

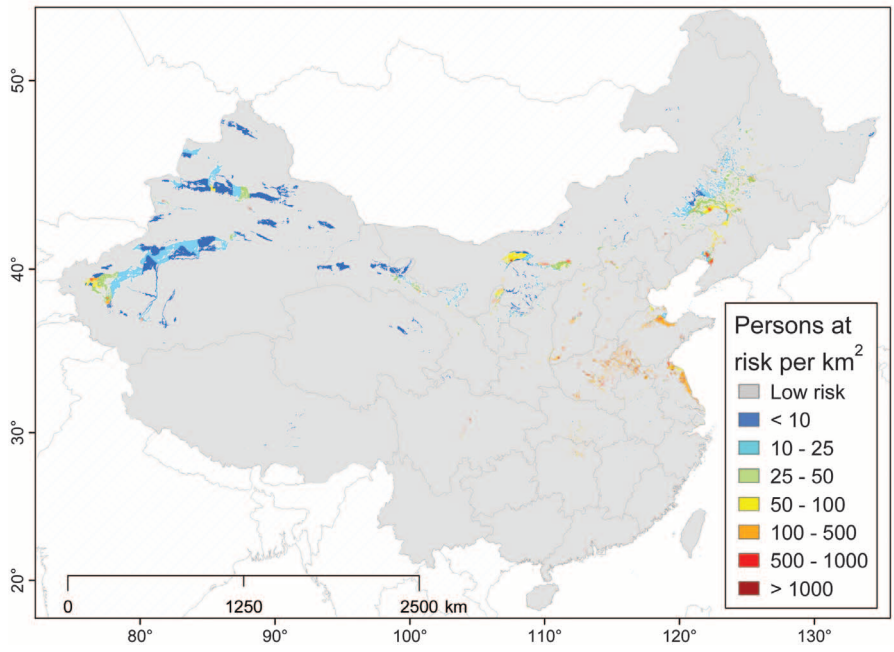

Fig. 3. Estimated Chinese population at potential risk of exposure to arsenic concentrations of >10 μg liter^{-1}. Calculation is based on the model results and population density estimates.

the actual population at risk, because treated and piped water may be used in some places, but water use statistics are not available. However, most of the arsenic-affected areas in China correspond to arid or semiarid regions, where groundwater is the predominant source of drinking water.

Our approach complements traditional groundwater quality surveys, which are expensive and time-consuming. The model requires only a small number of geospatial parameters to provide a preliminary assessment of affected areas, reducing the area that needs to be screened. It may also be appropriate for use in other parts of the world, especially in arid regions such as northwestern Argentina and Chile, where high arsenic concentrations have been reported, or in countries such as Mongolia, Kazakhstan, and Kyrgyzstan, where risk assessments for groundwater arsenic contamination have not yet been performed.

References and Notes

1. J. Qiu, *Science* **334**, 745–745 (2011).
2. G. Sun, *Toxicol. Appl. Pharmacol.* **198**, 268–271 (2004).
3. G. Sun, Y. Xu, Q. Zheng, S. Xi, *Kaohsiung J. Med. Sci.* **27**, 377–381 (2011).
4. J. X. Guo *et al.*, *J. Environ. Sci. Health A* **42**, 1853–1858 (2007).
5. S. Li, T. Xiao, B. Zheng, *Sci. Total Environ.* **421-422**, 31–40 (2012).
6. W. P. Tseng *et al.*, *J. Natl. Cancer Inst.* **40**, 453–463 (1968).
7. Y. Jin, C. Liang, G. He, J. Cao, *J. Hygiene Res.* **32**, 519–540 (2003).
8. J. Liu *et al.*, *Environ. Health Perspect.* **110**, 119–122 (2002).
9. P. L. Smedley, D. G. Kinniburgh, *Appl. Geochem.* **17**, 517–568 (2002).
10. Y. Deng, Y. Wang, T. Ma, *Appl. Geochem.* **24**, 587–599 (2009).
11. H. Guo, Y. Wang, *J. Geochem. Explor.* **87**, 109–120 (2005).
12. H. Guo, B. Zhang, G. Wang, Z. Shen, *Chem. Geol.* **270**, 117–125 (2010).
13. L. H. Zhang, Q. H. Guo, in *Water-Rock Interaction Volumes 1 & 2*, T. D. Bullen, Y. Wang, Eds. (Taylor & Francis, London, 2007), pp. 1299–1303.
14. P. L. Smedley, M. Zhang, G. Zhang, Z. Luo, *Appl. Geochem.* **18**, 1453–1477 (2003).
15. H. Hagiwara, J. Akai, K. Terasaki, T. Yoshimura, H. Luo, *Appl. Geochem.* **26**, 380–393 (2011).
16. X. Xie *et al.*, *Chemosphere* **90**, 1878–1884 (2013).
17. J.-J. Lee, C.-S. Jang, C.-W. Liu, C.-P. Liang, S.-W. Wang, *Environ. Sci. Technol.* **43**, 6662–6668 (2009).
18. M. Currell, I. Cartwright, M. Raveggi, D. Han, *Appl. Geochem.* **26**, 540–552 (2011).
19. W. M. Edmunds, J. Ma, W. Aeschbach-Hertig, R. Kipfer, D. P. F. Darbyshire, *Appl. Geochem.* **21**, 2148–2170 (2006).
20. B. E. O. Dochartaigh, A. M. MacDonald, *Groundwater Degradation in the Chahaertan Oasis, Alxa League, Inner Mongolia* (British Geological Survey, Nottingham, 2006).
21. G. Yu, D. Sun, Y. Zheng, *Environ. Health Perspect.* **115**, 636–642 (2007).
22. G. F. Sun *et al.*, in *Arsenic Exposure and Health Effects IV*, W. R. Chappell, C. O. Abernathy, R. L. Calderon, Eds. (Elsevier, Amsterdam, 2001), pp. 79–85.
23. M. Amini *et al.*, *Environ. Sci. Technol.* **42**, 3669–3675 (2008).
24. L. R. Lado, D. Polya, L. Winkel, M. Berg, A. Hegan, *Appl. Geochem.* **23**, 3010–3018 (2008).
25. L. Winkel, M. Berg, M. Amini, S. J. Hug, C. A. Johnson, *Nat. Geosci.* **1**, 536–542 (2008).
26. L. H. E. Winkel *et al.*, *Proc. Natl. Acad. Sci. U.S.A.* **108**, 1246–1251 (2011).
27. J. Bian, J. Tang, L. Zhang, H. Ma, J. Zhao, *J. Geochem. Explor.* **112**, 347–356 (2012).
28. S. Han, H. Zhang, M. Zhang, *Geochim. Cosmochim. Acta* **74**, A378 (2010).
29. M. N. Mead, *Environ. Health Perspect.* **113**, A378–A386 (2005).
30. Y. Xia, J. Liu, *Toxicology* **198**, 25–29 (2004).

Acknowledgments: Supported by the Sino-Swiss Science and Technology Cooperation Program of the Swiss State Secretariat for Education and Research (project IZLCZ2 123971), the National Science and Technology Pillar Program of China during the 11th Five-Year Plan Period (contract grant no. 2006BAI06B04), and the External Cooperation Program of the Chinese Academy of Sciences. We thank G.-B. Jiang and J. Shi of the Research Center for Eco-Environmental Sciences, Beijing, for support and data collection in the initial phase of the project. L.R.-L. also acknowledges the Isidro Parga Pondal research program from the Xunta de Galicia (Spain) for current financial support. Additional data are available at www.eawag.ch/repository/remarc.

Supplementary Materials

www.sciencemag.org/cgi/content/full/341/6148/866/DC1
Materials and Methods
Figs. S1 to S5
Tables S1 to S7
References (*31*–*50*)

6 March 2013; accepted 19 June 2013
10.1126/science.1237484

Hillslopes Record the Growth and Decay of Landscapes

Martin D. Hurst,[1,2]* Simon M. Mudd,[1] Mikael Attal,[1] George Hilley[3]

Earth's surface archives the combined history of tectonics and erosion, which tend to roughen landscapes, and sediment transport and deposition, which smooth them. We analyzed hillslope morphology in the tectonically active Dragon's Back Pressure Ridge in California, United States, to assess whether tectonic uplift history can be reconstructed using measurable attributes of hillslope features within landscapes. Hilltop curvature and hillslope relief mirror measured rates of vertical displacement caused by tectonic forcing, and their relationships are consistent with those expected when idealizing hillslope transport as a nonlinear diffusion process. Hilltop curvature lags behind relief in its response to changing erosion rates, allowing growing landscapes to be distinguished from decaying landscapes. Numerical modeling demonstrates that hillslope morphology may be used to infer changes in tectonic rates.

Hillslope morphology is a first-order indicator of landscape change, with great potential for investigating landscapes in tectonically active settings (*1*–*3*). Under the condition that erosion rates have adjusted to tectonic uplift, landscape morphology can be used to infer uplift rates (*4*). Until recently, efforts have focused on inferring rates of base-level fall from channel profiles; hillslopes were generally considered insensitive to rapid base-level fall because

they become invariantly steep and planar in such a context (*5*). Advances in the quality of digital topographic data have recently led to new techniques allowing interpretation of hillslope morphology as a first-order indicator of change in boundary conditions, even in rapidly uplifted landscapes (*1*–*3*). In the limiting case that channels respond more rapidly to changes in uplift rates than do hillslopes, the history of tectonic rates may be faithfully archived in the profile form of hillslopes (*6*). Hilltop curvature (C_{HT}) and mean hillslope gradient (S) are expected to vary predictably with relative base-level lowering rates (hereafter equated with tectonic uplift rate, U), provided that hilltops remain soil-mantled (*2*, *7*).

We studied hillslope morphology at the Dragon's Back Pressure Ridge (DBPR), located along the San Andreas Fault (SAF) in California, United States. Small catchments (<400 m long) trending perpendicular to the fault are cut into poorly consolidated sediments of the Paso Robles formation that are readily transportable as soil (*8*). Geological mapping reveals that these sediments are progressively folded as a monocline to the northwest. Surface structures exposed within the North American Plate and magnetotelluric profiles suggest that the SAF is offset in the shallow subsurface and that this offset remains stationary with respect to the North American Plate. Taken together, these observations indicate that flat-lying sediments southwest of the DBPR are progressively deformed as strike-slip motion moves them into and through the deformation zone created by this offset (Fig. 1A). Topography along the DBPR reflects translation through the fixed uplift zone at a rate equal to the mean slip rate along the SAF (33 mm year^{-1}), allowing a space-for-time substitution to analyze topography as a result of the integrated uplift history along the landform. As such, uplift increases rapidly from SE to NW along the landform, peaking 1200 m from the SE tip of the ridge [30 thousand years ago (ka)] and declining by 2000 m from that point (60 ka) (Fig. 1A) (*8*). Additionally, it has been demonstrated that the fluvial system rapidly communicates changes in uplift rates to hillslopes, which is a limiting condition required to examine hillslope responses to changing tectonic rates (*8*).

In steep, rapidly eroding terrain, hillslope gradient is often invariant (*5*, *9*), an observation consistent with geomorphic transport models in which sediment flux increases nonlinearly with hillslope gradient and tends to infinity as the gradient approaches a critical slope, S_C (*2*, *10*, *11*). When tectonic uplift is balanced by surface lowering rates (hereafter referred to as a steady-state relationship), a relationship can be derived from this flux law between two dimensionless topographic measures: (i) an apparent dimensionless erosion rate E^* and (ii) dimensionless relief R^* (*7*) (supplementary materials)

$$E^* = \frac{2C_{HT}L_H}{S_C} \quad (1)$$

$$R^* = \frac{S}{S_C};\ S < S_C \quad (2)$$

where L_H is horizontal hillslope length. Changes in E^* and R^* are primarily driven by changes in C_{HT} and S, respectively. As E^* becomes large, R^* asymptotically approaches unity, indicating that mean slopes approach S_C at high uplift rates (Fig. 2A, dashed line). When the steady-state assumption is violated, deviation from the steady-state relationship (Fig. 2A, dashed line) has been hypothesized to reflect the adjustment of hillslope profiles to changes in relative base-level lowering rates (*6*). Therefore, we calculate E^* and R^* from high-resolution topographic data (see the supplementary materials for details) by quantifying S, C_{HT}, and L_H to reveal landscape history in relation to changing uplift (*2*).

S, C_{HT}, and L_H all increase in response to increased erosion rates (Fig. 1). S attains maximum values by 900 m (27 ka) along the landform and remains high until 2700 m (82 ka), suggesting that S is limited by landsliding in these areas as previously observed (*8*). By 750 m (23 ka), L_H increases to 30 m and remains approximately constant until 2700 m (82 ka). Uplift rates are high (>1 mm year^{-1}) at 900 to 1800 m (27 to 55 ka); in this zone, C_{HT} increases to a maximum value 750 m (23 ka) after uplift has declined.

We used S, C_{HT}, and L_H to calculate E^* and R^*, fixing $S_C = 0.8$ so that R^* cannot exceed unity (S should not exceed S_C). We observed systematic deviations between the measured values and those expected for steady-state hillslopes (Fig. 2A). Initially, increasing S elevates R^* and increasing L_H and C_{HT} causes E^* to rise. R^* does not notably

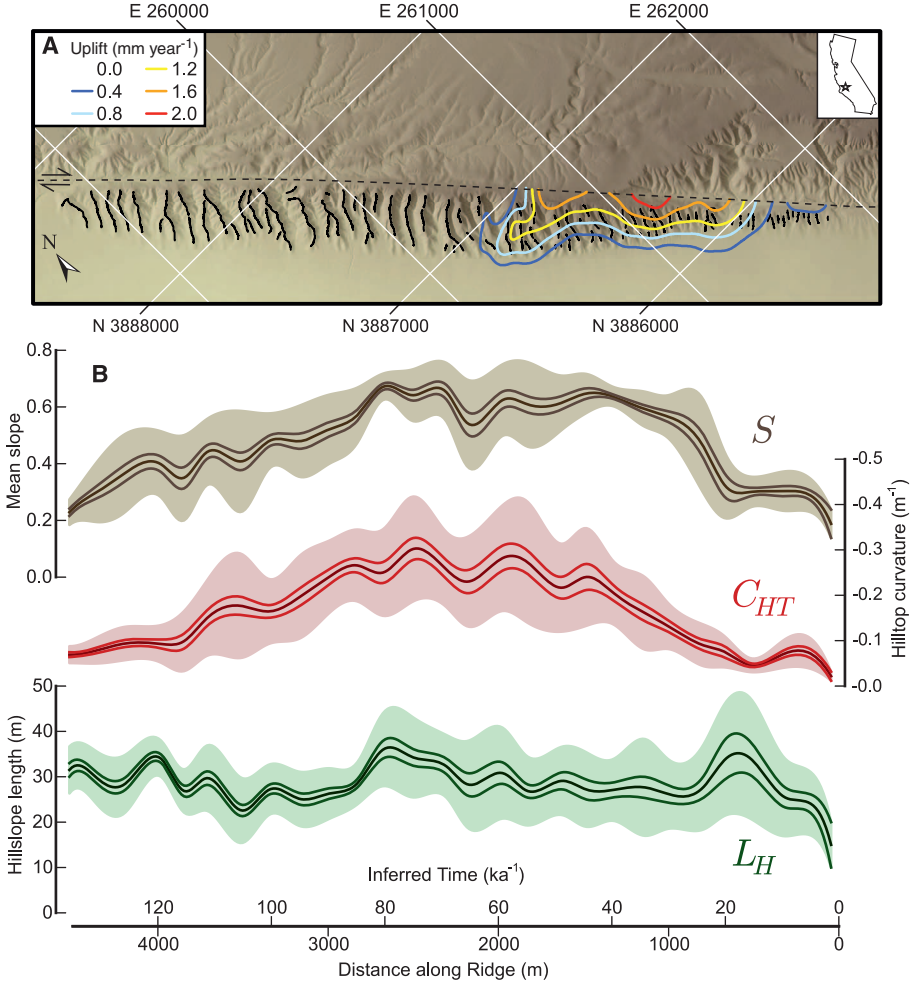

Fig. 1. Study site and hillslope morphology. (**A**) Shaded relief image of the DBPR adjacent to the SAF [Universal Transverse Mercator zone, 11N projection; with eastings (E) and northings (N) given in meters]. Contours show the distribution of surface uplift derived by geological mapping of deformed sedimentary beds (*8*), and black lines depict mapped hilltops. (**B**) Distribution of surface metrics sampled from hilltops in (A). Shaded regions show standard deviations, and solid lines are standard errors about bin means. The space-for-time substitution is based on a slip rate of 0.033 m year^{-1} on the SAF (*8*). S appears limited by 900 m along the DBPR, whereas C_{HT} continues to increase, suggesting rising erosion rates.

[1]School of Geosciences, University of Edinburgh, Drummond Street, Edinburgh EH8 9XP, UK. [2]British Geological Survey, Keyworth, Nottingham NG12 5GG, UK. [3]Department of Geological and Environmental Sciences, Stanford University, 397 Panama Mall, Stanford, CA 94305–2210, USA.

*Corresponding author. E-mail: mhurst@bgs.ac.uk

increase after 25 ka as hillslope gradient approaches S_C. Increasing C_{HT} raises E^* even after uplift ceases at 55 ka. From 80 ka onward, both E^* and R^* decline gradually; however, E^* values are larger for a given R^* value than would be predicted based on the steady-state model. This pattern suggests that changes in C_{HT} (and hence E^*) lag behind S (and hence R^*). The result is tectonically induced hysteresis in hillslope form: high-relief, low-C_{HT} and low-relief, high-C_{HT} hillslopes are associated with active and waning tectonic uplift, respectively.

We constructed a one-dimensional numerical model of hillslope evolution to determine whether the observed hysteresis could be explained by the lag in hillslope response to changes in base-level lowering rates (supplementary materials). The model used a time-dependent uplift pulse idealized as a Gaussian function with the timing (t_{max}*), standard deviation (t_{std}*), and magnitude (U_{max}*) of uplift treated as model parameters. L_H and the transport coefficient D (supplementary materials) were fixed for the modeled hillslope. A Monte Carlo approach was used to find the most likely combination of these parameters according to the misfit between values of R^* and E^* derived from the DBPR topography and those calculated at corresponding model-time values in the forward model.

The resulting distribution of apparent uplift is shown in Fig. 3A. Dimensionalization of the best-fit modeled uplift field uses $D = 0.0086$ m^2 year^{-1} as previously derived for the study site (*12*), and the similarity in magnitude of modeled U with the independently derived mapped uplift field (*8*) supports this value. The model reasonably explains the distribution of hillslope morphology, as shown by the similarity between E^* derived from topography and the modeled hillslope through time (Fig. 3B). Although first-order features of hillslopes within the DBPR were captured using the model, several key features remain unexplained.

First, the inferred U^* distribution implicitly equates changes in base-level lowering rate with changes in rock uplift rate. Channels adjust rapidly but not instantaneously to the waning of uplift (*8*). This delayed channel response introduces an additional 15 to 20 ka ($t^* = 0.14$ to 0.19) lag between changes in uplift and relative base-level fall along hillslopes, similar to the offset between their mapped uplift field and the most likely distribution of U^* derived from the model (Fig. 3A). The modeled t_{std}* values were larger than those observed, with apparent uplift distributed throughout the model run (Fig. 3A).

Second, peak E^* values are smaller than E^* derived from the topography (Fig. 3B). This probably reflects the choice of a modeled Gaussian uplift pulse that is smoother than the documented uplift distribution at the DBPR.

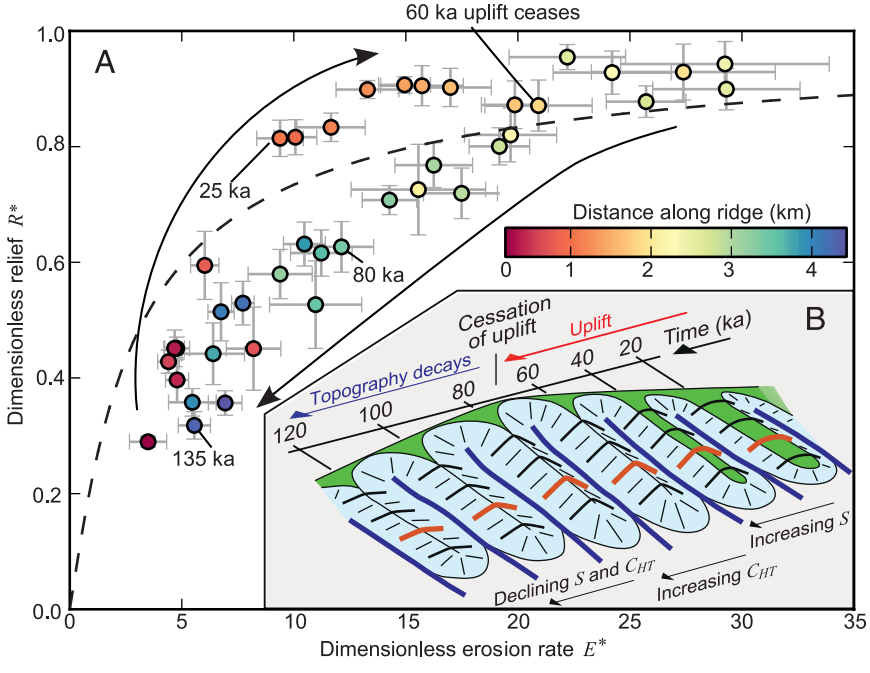

Fig. 2. Hysteresis in hillslope morphology. (**A**) Variation in E^* and R^* with distance toward the NW along the DBPR. The dashed line indicates the theoretical relationship for steady-state hillslopes. Error bars are propagated from standard errors in Fig. 1. The space-for-time substitution is based on a slip rate of 0.033 m a^{-1} on the SAF (*8*). The morphological evolution of hillslopes is distinct for adjustment during uplift versus relaxation after uplift has ceased. (**B**) Schematic diagram illustrating landscape response to the onset and conclusion of uplift and the expected distribution of E^* versus R^*. Values for E^* versus R^* reflect hillslope profiles highlighted in red on the schematic plot. Uplift triggers increased erosion rates in channels that dissect the original surface. A wavelike signal propagates onto the hillslopes, causing steepening (20 to 40 ka). Subsequently, the hilltops respond by becoming sharper (60 to 80 ka). At 60 ka, uplift ceases and channel slopes decrease (*8*). Hillslope gradients and hilltop curvature both reduce gradually in response.

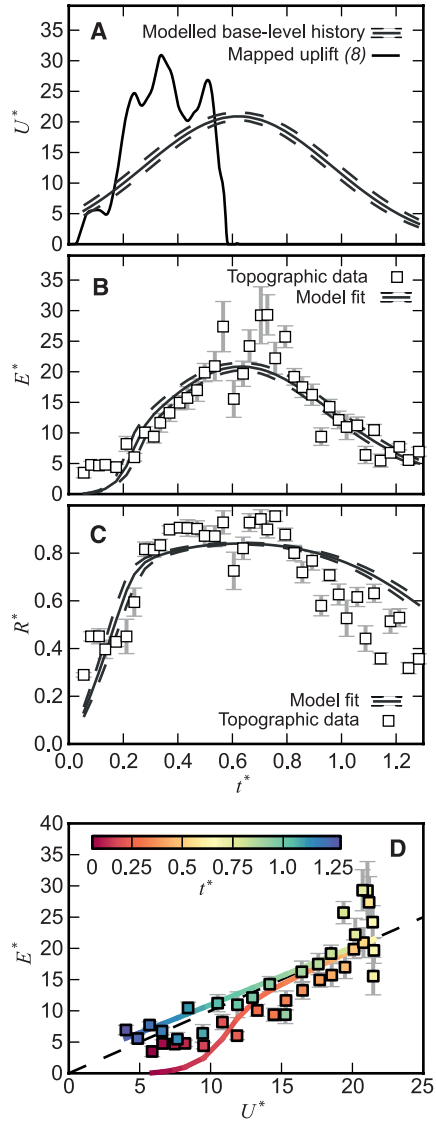

Fig. 3. Modeled uplift. (**A**) Distribution of U^* as a function of t^*. The solid black line represents the mapped uplift field normalized according to eq. S3C (using $D = 0.0086$ m^2 year^{-1} (*12*) and $L_H = 30$ m) and a slip rate of 0.033 m year^{-1}. The gray line is the Gaussian function for apparent uplift (base-level fall), providing the best fit to observed topography from probability densities with mean values (±1σ) of U_{max}* = 20.89 (±0.6), t_{max}* = 0.621 (±0.001), and t_{std}* = 0.490 (±0.015). (**B**) Distribution of E^* through t^*: topography-derived (eq. 5SB) and modeled E^* (Pearson's correlation test gives $R^2 = 0.78$). (**C**) Distribution of modeled and measured R^* through t^*. (**D**) E^* from topography and modeled hillslopes as a function of model-derived apparent uplift U^* through t^*. Hysteresis is recorded so that during accelerating uplift and topographic growth E^* lags behind U^*, whereas during landscape relaxation E^* lags behind a declining U^*.

Third, toward the NW end of the DBPR [beyond 2700 m (80 ka)], R^* is generally smaller than model predictions (Fig. 3C). The mismatch could be due to high transport rates in the study area associated with processes that are not replicated in the model, such as debris flows, landslides, and erosion by overland flow (fig. S2), which have been interpreted as a possible cause for variation in channel concavities within and beyond the uplift zone (*8*).

Finally, we integrated the modeling results with field observations in a conceptual framework for the temporal evolution of the DBPR (Fig. 2B). Accelerated uplift drives erosional adjustment that propagates into a landscape. Channel erosion ensues, with a concomitant delay in hillslope response, so relief can grow without a commensurate change in C_{HT} and thus E^*, leading to data lying above the steady-state E^* versus R^* curve. Once uplift stops, channels rapidly become gentler (*8*), whereas again hillslopes and hilltops are slower to respond, leading to points lying below the steady E^* versus R^* curve. This hysteresis has important implications for the interpretation of transient hillslopes, providing a means to discriminate between growing and decaying landscapes based on hillslope topography alone.

Our findings highlight the potential to distinguish active faults in remote settings, quantify the distribution of fault-related uplift, and delineate zones with high landslide risk (i.e., zones with high uplift rate, steep landscape, and/or proximity to active faults). Such an approach will be best suited to landscapes where hillslopes have a response time that is longer than that of the channel network, but not so long that channels effectively become decoupled from their base level. Alternatively, where the response time of the channel network is very long, hillslopes may be able to track spatial variation in relative base levels (*2*) and provide a complementary test to channel-based erosion rate metrics.

References and Notes

1. R. A. DiBiase, A. M. Heimsath, K. X. Whipple, *Earth Surf. Process. Landf.* **37**, 855–865 (2012).
2. M. D. Hurst, S. M. Mudd, R. Walcott, M. Attal, K. Yoo, *J. Geophys. Res. Earth Surf.* **117**, F02017 (2012).
3. M. D. Hurst, S. M. Mudd, K. Yoo, M. Attal, R. Walcott, *J. Geophys. Res. Earth Surface* **118**, 832 (2013).
4. A. C. Whittaker, *Lithosphere* **4**, 160–164 (2012).
5. R. A. DiBiase, K. X. Whipple, A. M. Heimsath, W. B. Ouimet, *Earth Planet. Sci. Lett.* **289**, 134–144 (2010).
6. S. M. Mudd, D. J. Furbish, *J. Geophys. Res. Earth Surf.* **112**, F03S18 (2007).
7. J. J. Roering, J. T. Perron, J. W. Kirchner, *Earth Planet. Sci. Lett.* **264**, 245–258 (2007).
8. G. E. Hilley, J. R. Arrowsmith, *Calif. Geol.* **36**, 367 (2008).
9. S. A. Binnie, W. M. Phillips, M. A. Summerfield, L. K. Fifield, *Geology* **35**, 743 (2007).
10. D. J. Andrews, R. C. Bucknam, *J. Geophys. Res.* **92**, 12857 (1987).
11. J. J. Roering, J. W. Kirchner, W. E. Dietrich, *Water Resour. Res.* **35**, 853–870 (1999).
12. J. R. Arrowsmith, D. D. Rhodes, D. D. Pollard, *J. Geophys. Res.* **103**, 10141 (1998).

Acknowledgments: This work was supported by a National Environmental Research Council grant (NE/G524128/1) awarded to M.D.H. and by grant NE/H001174/1 and a grant from the Carnegie Trust for the Universities of Scotland to S.M.M.. Thanks to J. Roering, D. Lague, and M. Ellis for helpful discussions. Three anonymous reviewers provided comments that greatly improved the manuscript. Data are available in either the supplementary materials or at the Community Surface Dynamics Modeling System (http://csdms.colorado.edu/wiki/Main_Page).]

Supplementary Materials

www.sciencemag.org/cgi/content/full/341/6148/868/DC1
Materials and Methods
Figs. S1 to S4
References (*13*–*19*)

11 June 2013; accepted 30 July 2013
10.1126/science.1241791

Mapping Tectonic Deformation in the Crust and Upper Mantle Beneath Europe and the North Atlantic Ocean

Hejun Zhu[1]* and Jeroen Tromp[1,2]

We constructed a three-dimensional azimuthally anisotropic model of Europe and the North Atlantic Ocean based on adjoint seismic tomography. Several features are well correlated with historical tectonic events in this region, such as extension along the North Atlantic Ridge, trench retreat in the Mediterranean, and counterclockwise rotation of the Anatolian Plate. Beneath northeastern Europe, the direction of the fast anisotropic axis follows trends of ancient rift systems older than 350 million years, suggesting "frozen-in" anisotropy related to the formation of the craton. Local anisotropic strength profiles identify the brittle-ductile transitions in lithospheric strength. In continental regions, these profiles also identify the lower crust, characterized by ductile flow. The observed anisotropic fabric is generally consistent with the current surface strain rate measured by geodetic surveys.

Minerals that constitute the Earth's crust and upper mantle, such as amphibole and olivine, are highly anisotropic in terms of seismic wavespeeds. Deformation induced by tectonic activity can align the fast axes of these minerals with the directions of flow or principal extension (*1*). This process of lattice preferred orientation leads to a directional and polarization dependence of seismic wavespeeds. Seismic anisotropy has been observed within the crust, lithosphere, and asthenosphere at various scales (*2*–*6*), providing important constraints on past and present deformation within Earth's interior (*7*–*9*).

The European continent has undergone extensive tectonic deformation since the Archaean and was especially heavily reworked by Meso-Cenozoic volcanism and subduction (*10*, *11*). Geodetic surveys have detected substantial deformation due to the convergence of the Eurasian, African, and Arabian Plates (*12*). Most seismic studies in this area have focused on mapping lateral heterogeneities in compressional (*11*) and shear wavespeeds (*13*). Anisotropic images either come from investigations at the global scale (*14*) or local studies limited to a relatively small region (*6*).

Here we present an azimuthally anisotropic model of Europe and the North Atlantic Ocean, constructed based on adjoint tomography. We collected 26,581 three-component seismograms from 190 earthquakes recorded by 745 seismographic stations (supplementary text S1). We used spectral-element (*15*) and adjoint methods (*16*–*18*) to numerically calculate synthetic seismograms and Fréchet derivatives with respect to radial and azimuthal anisotropic model parameters (*19*, *20*) in fully three-dimensional (3D) Earth models (supplementary text S4). Frequency-dependent phase and amplitude measurements of three-component surface waves with periods between 25 and 100 s were used to constrain structure at depths shallower than 200 to 250 km (supplementary text S3). A new anisotropic model of Europe and the North Atlantic Ocean, called EU_{60}, was obtained after 10 preconditioned conjugate gradient iterations (*21*).

Both isotropic shear wavespeed and the anisotropic fast axis reveal numerous features correlated with tectonic activity in the region (Fig. 1). Along the North Atlantic Ridge (NAR), the shear wavespeed is relatively slow (<−3%) down to a depth of 250 km. The fast axis is perpendicular to the ridge system, in agreement with the extensional direction of this divergent plate boundary.

In the western Mediterranean, the east-west–oriented fast direction runs parallel to the opening trajectory of the Algero-Provençal and Tyrrhenian Seas, induced by slab roll-back and migration of the Calabrian and Apennines arcs starting ~30 million years ago (*11*). This strong azimuthal anisotropy correlates with a large shear wavespeed reduction (~−4%) down to depths in excess of 200 km, suggesting intensive deformation and asthenospheric flow associated with trench

[1]Department of Geosciences, Princeton University, Princeton, NJ, USA. [2]Program in Applied and Computational Mathematics, Princeton University, Princeton, NJ, USA.

*Corresponding author. E-mail: hejunzhu@princeton.edu